

# Bifunctional nanoprecipitates strengthen and ductilize a medium-entropy alloy

<https://doi.org/10.1038/s41586-021-03607-y>

Received: 26 August 2019

Accepted: 4 May 2021

Published online: 7 July 2021

 Check for updates

Ying Yang<sup>1</sup>✉, Tianyi Chen<sup>1,5</sup>, Lizhen Tan<sup>1</sup>, Jonathan D. Poplawsky<sup>2</sup>, Ke An<sup>3</sup>, Yanli Wang<sup>1</sup>, German D. Samolyuk<sup>1</sup>, Ken Littrell<sup>3</sup>, Andrew R. Lupini<sup>2</sup>, Albina Borisevich<sup>2</sup> & Easo P. George<sup>1,4</sup>✉

Single-phase high- and medium-entropy alloys with face-centred cubic (fcc) structure can exhibit high tensile ductility<sup>1,2</sup> and excellent toughness<sup>2,3</sup>, but their room-temperature strengths are low<sup>1–3</sup>. Dislocation obstacles such as grain boundaries<sup>4</sup>, twin boundaries<sup>5</sup>, solute atoms<sup>6</sup> and precipitates<sup>7–9</sup> can increase strength. However, with few exceptions<sup>8–11</sup>, such obstacles tend to decrease ductility. Interestingly, precipitates can also hinder phase transformations<sup>12,13</sup>. Here, using a model, precipitate-strengthened, Fe–Ni–Al–Ti medium-entropy alloy, we demonstrate a strategy that combines these dual functions in a single alloy. The nanoprecipitates in our alloy, in addition to providing conventional strengthening of the matrix, also modulate its transformation from fcc-austenite to body-centred cubic (bcc) martensite, constraining it to remain as metastable fcc after quenching through the transformation temperature. During subsequent tensile testing, the matrix progressively transforms to bcc-martensite, enabling substantial increases in strength, work hardening and ductility. This use of nanoprecipitates exploits synergies between precipitation strengthening and transformation-induced plasticity, resulting in simultaneous enhancement of tensile strength and uniform elongation. Our findings demonstrate how synergistic deformation mechanisms can be deliberately activated, exactly when needed, by altering precipitate characteristics (such as size, spacing, and so on), along with the chemical driving force for phase transformation, to optimize strength and ductility.

The concept underlying our strategy can be illustrated with two hypothetical alloys. Alloy A1 is single-phase fcc (austenite) at elevated temperatures, Fig. 1a. Its composition is such that, when quenched to room temperature, it should undergo a transformation to bcc-martensite, Fig. 1b. Alloy A2 has a two-phase microstructure at elevated temperatures, Fig. 1c, comprising precipitates distributed in a fcc-austenite matrix whose composition is identical to A1. Therefore, in the absence of precipitates, the A2 matrix should also undergo a transformation to bcc-martensite when quenched. However, on account of the spatial confinement imposed by the precipitates, we expect its martensitic transformation to be suppressed, resulting in a matrix that is metastable fcc-austenite, Fig. 1d.

To realize these alloys, we designed and fabricated two medium-entropy alloy (MEA) compositions. First, the A2 alloy, which has the composition Fe–32.6Ni–6.1Al–2.9Ti (at%), and is denoted henceforth as FNAT-47h after its main constituents and ageing time (47 h). Thermodynamic calculations (Extended Data Fig. 1a, b) indicated that, after solutionizing at 1,100 °C and ageing at 700 °C for 47 h, the equilibrium phases in this alloy should be a fcc matrix with the approximate composition Fe–23Ni–3.5Al–0.5Ti (at%) containing Ni<sub>3</sub>Al (L1<sub>2</sub>)-type precipitates. For this matrix composition, it is estimated that bcc is more stable

than fcc below approximately 500 °C (first-principles energy calculations, Extended Data Fig. 1c), and the martensite start and finish temperatures are 200 and 25 °C, respectively<sup>14</sup>. Second, the A1 alloy, which has the same composition as the matrix of the FNAT-47h alloy at 700 °C and is denoted henceforth as FNAT-m-47h. Both alloys were processed and heat-treated the same way. As expected, the FNAT-m-47h alloy was almost fully martensitic after quenching into water at room temperature (approximately 21 °C throughout this Article) (Fig. 1e); small-angle neutron scattering (SANS) measurements found no evidence of nanoprecipitates (Fig. 1f). By contrast, the precipitate-containing FNAT-47h alloy after water-quenching consists of a predominantly fcc matrix (red) containing a few isolated bcc regions (green); see the electron backscattered diffraction (EBSD) image, Fig. 1g. SANS measurements (Fig. 1h) confirmed the presence of approximately 24 vol% nanoprecipitates with an average radius of 10.4 nm and a number density of  $4.3 \times 10^{22} \text{ m}^{-3}$  (Extended Data Table 1). The mostly fcc matrix of FNAT-47h must therefore be due to the nanoprecipitates in this alloy hindering the otherwise favoured fcc-to-bcc martensitic transformation. This is a fundamental difference relative to previous works<sup>8,9,15,16</sup>, where the role of precipitates was to strengthen and not to suppress martensite formation.

<sup>1</sup>Materials Science and Technology Division, Oak Ridge National Laboratory, Oak Ridge, TN, USA. <sup>2</sup>Center for Nanophase Materials Sciences, Oak Ridge National Laboratory, Oak Ridge, TN, USA. <sup>3</sup>Neutron Scattering Division, Oak Ridge National Laboratory, Oak Ridge, TN, USA. <sup>4</sup>Materials Science and Engineering Department, University of Tennessee, Knoxville, TN, USA.

<sup>5</sup>Present address: Oregon State University, Corvallis, OR, USA. ✉e-mail: yangying@ornl.gov; georgeep@ornl.gov

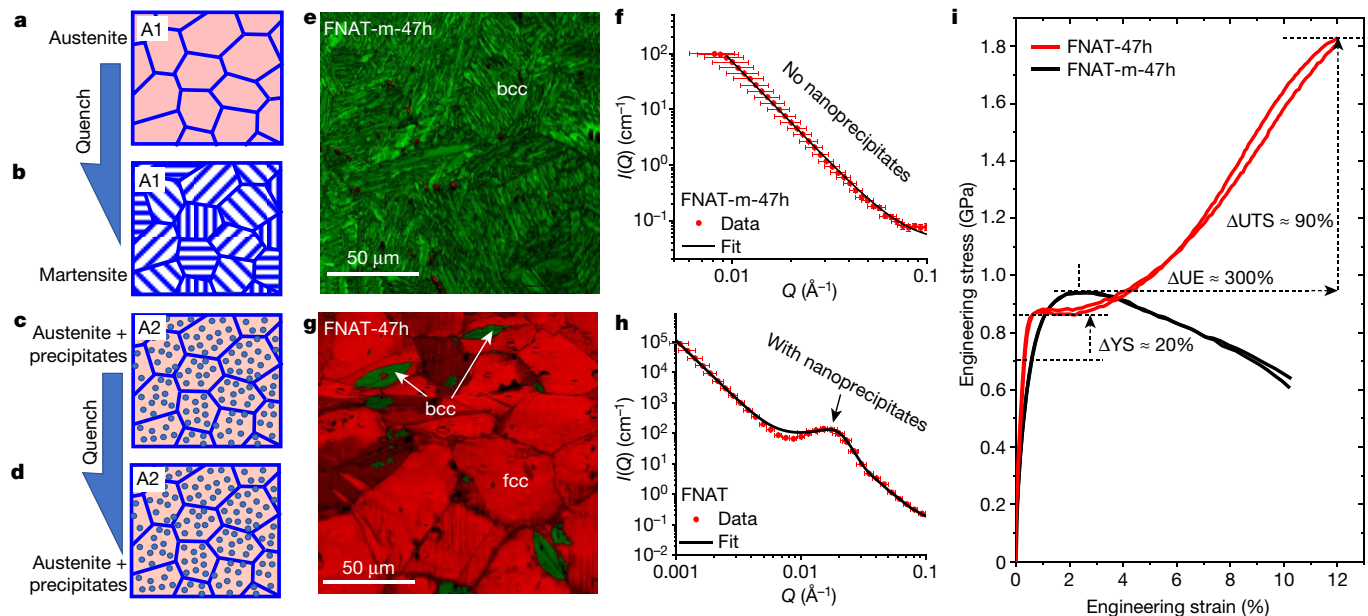


**Fig. 1 | Microstructures and tensile properties of FNAT-m-47h and FNAT-47h alloys.** **a–d**, Schematic drawings showing austenite without precipitates at elevated temperatures (A1; **a**); transformed martensite after quenching to room temperature (A1; **b**); austenite plus precipitates at elevated temperatures (A2; **c**); and retained austenite plus precipitates after quenching to room temperature (A2; **d**). **e**, EBSD image quality and phase map showing the fully martensitic structure of FNAT-m-47h after water quenching. **f**, SANS plot of scattered intensity versus inverse wavelength showing no evidence of nanoprecipitates in FNAT-m-47h; error bars represent 1 standard deviation.

**g**, EBSD image quality and phase map showing equiaxed fcc (red) and lenticular bcc (green) regions in FNAT-47h after water quenching. **h**, SANS plot showing a hump corresponding to the nanoprecipitates in FNAT-47h; error bars represent 1 standard deviation. **i**, Examples of engineering stress–strain curves of as-quenched FNAT-m-47h and FNAT-47h alloys tensile-tested at room temperature;  $\Delta\text{UTS}$ ,  $\Delta\text{UE}$  and  $\Delta\text{YS}$  represent, respectively, the increase in the ultimate tensile strength (UTS), uniform elongation (UE) and yield strength (YS).

Room-temperature tensile tests were performed on the as-quenched FNAT-47h and FNAT-m-47h alloys. The yield strength (YS), ultimate tensile strength (UTS) and uniform elongation (UE) of FNAT-47h are approximately 20%, 90% and 300% higher than those of FNAT-m-47h, Fig. 1*i*. The strengthening effect of the nanoprecipitates in FNAT-47h is higher than implied above because the matrix of FNAT-m-47h is bcc-martensite, which is inherently stronger than the fcc matrix of FNAT-47h. To evaluate the yield strength of the fcc matrix, we tested FNAT-47h in the solutionized state and found it to be approximately 325 MPa (Extended Data Fig. 2a). Additionally, there is a small contribution from the approximately 4 vol% bcc-martensite in FNAT-47h (Fig. 1*g*), which can be estimated from the yield strength of FNAT-m-47h (~705 MPa, Fig. 1*i*). From a simple rule-of-mixtures addition of the contributions of the different phases the yield strength of FNAT-47h is estimated as approximately 883 MPa, where a large contribution is from the nanoprecipitates, about 535 MPa (Methods section ‘Tensile testing and mechanical properties’ provides details and uncertainties). This estimated yield strength is comparable to the measured value,  $862 \pm 6$  MPa (mean  $\pm$  1 standard deviation throughout this Article, unless specified otherwise).

Microstructural results of FNAT-47h are shown in Fig. 2a–f. Atom probe tomography (APT), Fig. 2a, b, revealed spheroidal  $\text{L}_1_2$  precipitates (composition: Ni–13.8Al–6.6Fe–11.6Ti, at%) uniformly distributed in a fcc matrix (composition: Fe–3.6Al–22.3Ni–0.4Ti, at%). The precipitate volume fraction, number density, and mean radius are 0.26,  $3 \times 10^{22} \text{ m}^{-3}$ , and 10.2 nm, respectively. Similar precipitates are present also in the bcc regions of FNAT-47h (Extended Data Table 2). Within experimental uncertainty, (i) the compositions of the bcc and fcc regions are the same, and (ii) the nanoprecipitates in both regions have the same composition, size and number density. The APT compositions suggest these precipitates are of  $(\text{Ni}, \text{Fe})_3(\text{Al}, \text{Ti})$  type. Neutron diffraction (Fig. 2c) revealed fcc,  $\text{L}_1_2$  and bcc peaks. From Rietveld refinement of

high-resolution neutron diffraction data, the volume fractions of bcc,  $\text{L}_1_2$  and fcc phases were determined to be approximately 0.04, 0.28 and 0.68, respectively.

Transmission electron microscopy (TEM) results, Fig. 2d–f, indicate the presence of nanoscale bcc domains inside the fcc grains of FNAT-47h. Selected-area electron diffraction (SAED) revealed spots corresponding to the fcc matrix,  $\text{L}_1_2$  precipitates and bcc (Fig. 2d). A cube-on-cube relationship between the fcc matrix and the  $\text{L}_1_2$  precipitates in a [110] zone axis is indicated by the orange dotted lines and circles, respectively. The superposition of the bcc spots in the [100] zone axis (white dashed lines) on the fcc pattern (orange dotted lines) indicates a Nishiyama–Wasserman orientation relationship<sup>17</sup>. A scanning transmission electron microscopy (STEM) high-angle annular dark-field (HAADF) image (Fig. 2e) was taken to capture the detailed microstructure of an  $\text{L}_1_2$  precipitate and its surroundings. The Fourier-filtered image of Fig. 2e in Fig. 2f shows that the  $\text{L}_1_2$  precipitate at the centre (green) is contiguous with not only the fcc matrix (blue) but also a nanoscale bcc domain (red) in the fcc grain. Details of the orientation relationships, lattice misfits, and coherency of the  $\text{L}_1_2$ -bcc and  $\text{L}_1_2$ -fcc interfaces are illustrated in Extended Data Fig. 3a, b.

The  $\text{L}_1_2$  nanoprecipitates largely, but not fully, suppress the coarse-scale transformation of FNAT-47h from austenite to martensite during quenching. This can be compared to the effect of austenite grain boundaries. It is known that finer austenite grains decrease the martensite start temperature<sup>18–20</sup>,  $M_s$ . Fisher et al.<sup>18</sup> attributed the size effect of prior austenite grains to the so-called geometric partitioning process. Based on that, a roughly inverse linear relationship between the decrease in  $M_s$  relative to its reference value at infinite grain size and the logarithm of the austenite grain size has been obtained for several alloys, including Fe–Ni-based alloys<sup>20</sup>. Here, rather than the austenite grain size, presumably it is the spacing between precipitates that is the controlling length scale.

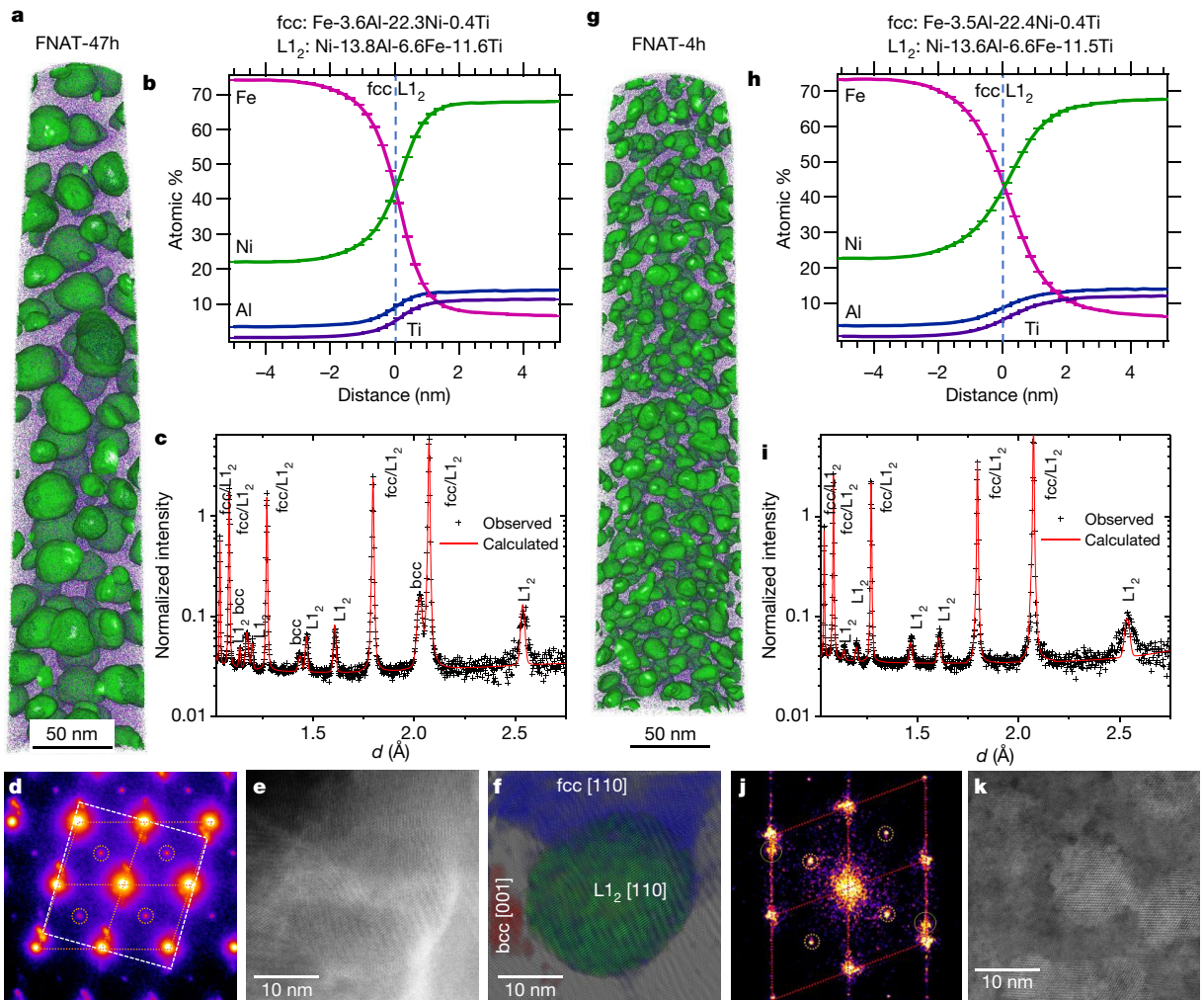


**Fig. 2 | Microstructure analysis of the FNAT-47h and FNAT-4h alloys.**

**a, b**, APT results from fcc grains of FNAT-47h showing the distribution and composition of L<sub>1</sub><sub>2</sub> precipitates in fcc matrix. **c**, High-resolution neutron diffraction pattern of FNAT-47h. Black crosses indicate observations, red line represents the calculated fit by Rietveld refinement. **d–f**, TEM results of FNAT-47h. **d**, SAED pattern where the orange dotted lines and circles indicate fcc and L<sub>1</sub><sub>2</sub> spots in a [110] zone, and the white dashed lines connect bcc spots in a [100] zone. **e**, STEM-HAADF image showing an L<sub>1</sub><sub>2</sub> precipitate embedded in the fcc

matrix. **f**, Fourier-filtered image of **e** showing L<sub>1</sub><sub>2</sub> (green), fcc (blue), and bcc (red) regions. **g, h**, APT results of FNAT-4h showing distribution and composition of L<sub>1</sub><sub>2</sub> precipitates in fcc matrix. **i**, High-resolution neutron diffraction pattern of FNAT-4h. Black crosses indicate observations, red line represents the calculated fit by Rietveld refinement. **j, k**, TEM results of FNAT-4h. **j**, SAED pattern with red dotted lines and circles indicating fcc and L<sub>1</sub><sub>2</sub> spots in a [110] zone. **k**, STEM-HAADF image showing an L<sub>1</sub><sub>2</sub> precipitate embedded in the fcc matrix.

To investigate the effect of precipitate spacing, we examined the microstructure after a shorter ageing time of 4 h at 700 °C (FNAT-4h) and quenched the same way after ageing as FNAT-47h. APT shows that the L<sub>1</sub><sub>2</sub> precipitates and fcc matrix in FNAT-4h have compositions and volume fractions (Fig. 2g, h) similar to those of FNAT-47h (Fig. 2a, b), suggesting that chemical equilibrium is reached already at 4 h. Since both alloys have the same matrix composition, they have the same chemical driving force for martensitic transformation. The only difference is that the shorter annealing time of FNAT-4h results in a higher density of smaller precipitates: number density of approximately  $6 \times 10^{23} \text{ m}^{-3}$  and mean radius of approximately 5.7 nm. Correspondingly, the precipitate spacing in FNAT-4h is approximately 12 nm compared to approximately 30 nm in FNAT-47h. From a spatial confinement viewpoint, therefore, we expected a lower tendency for martensite formation in FNAT-4h than in FNAT-47h. Consistent with this, no bcc peaks are discernible in the neutron diffraction spectrum of FNAT-4h (Fig. 2i), whereas bcc peaks (~4 vol%) are clearly visible in the spectrum of FNAT-47h (Fig. 2c). TEM analysis on FNAT-4h found no evidence of bcc reflections, as shown in the representative SAED image ([110] zone axis)

in Fig. 2j and the corresponding HAADF STEM image in Fig. 2k. What appear at first glance to be extra reflections (yellow circles in Fig. 2j) are the result of small variable local misorientations, as explained in Extended Data Fig. 4. The absence of bcc nanodomains in FNAT-4h suggests that, with increased spatial confinement, the formation of thermal martensite becomes nucleation-limited. On the other hand, their presence in FNAT-47h suggests that, as the spacing between precipitates increases, the process becomes growth-limited. When the constraint due to precipitates vanishes (as in FNAT-m-47h), the fcc phase transforms almost completely to martensite during quenching.

We next address the plastic deformation behaviour of the FNAT alloys and the multiple deformation mechanisms enabled by its unique microstructural features. Representative engineering stress–strain curves of FNAT annealed for 47 h, 8 h and 4 h are shown in Fig. 3a. True stress–strain curves of samples annealed for 47 h and 4 h, along with their work hardening rates (WHR), are shown in Fig. 3b, c, respectively. The microstructural changes occurring during plastic deformation were investigated by interrupting tensile tests at different strains and performing neutron diffraction; the corresponding spectra are shown in Fig. 3d, e.

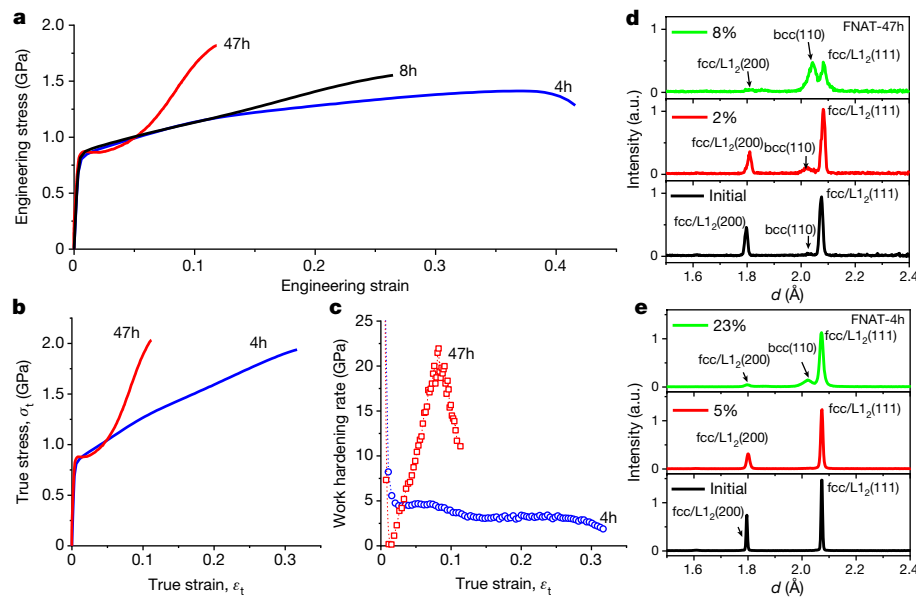


**Fig. 3 | Room-temperature mechanical properties and deformation mechanisms of FNAT alloys.** **a**, Engineering stress–strain curves of FNAT annealed at 700 °C for 47 h (red), 8 h (black) and 4 h (blue). **b**, True stress–strain curves of FNAT-47h and FNAT-4h. **c**, Work hardening rate versus true strain for

FNAT-47h and FNAT-4h. **d**, Neutron diffraction patterns from tensile tested samples of FNAT-47h interrupted at true strains of 0% ('Initial'), 2% and 8%. **e**, Neutron diffraction patterns from tensile tested samples of FNAT-4h interrupted at true strains of 0% ('Initial'), 5% and 23%.

After yielding at approximately 868 MPa, the tensile stress–strain curve of FNAT-47h drops slightly and then remains relatively flat up to a plastic strain of around 2%. Beyond that, there is a sharp increase in the WHR up to a plastic strain of approximately 8% followed by a sharp decrease up to the fracture strain of about 12%. Before loading, the diffraction spectrum ('Initial') consists mainly of fcc and L1<sub>2</sub> peaks, which overlap because of their small lattice mismatch, along with a small bcc (110) peak; these are the same three phases present in the alloy after heat treatment (Fig. 2c). With increasing applied strain (~2%), the intensity of the bcc (110) peak increases, whereas that of the fcc (111) peak does not decrease, which is probably due to an increase in {111} slip-induced texture that compensates for the intensity loss from the decreasing amount of fcc phase. At a larger strain (~8%), all the fcc/L1<sub>2</sub> peaks become smaller, and there remains a very small amount (~0.05 volume fraction) of fcc in the microstructure (Fig. 3d). After even larger strains, when the matrix has largely transformed from fcc to bcc, slip propagation through the different phases is accompanied by stacking faults in the L1<sub>2</sub> precipitates (Extended Data Fig. 3c–e).

The yield strength (~807 MPa) of FNAT-4h is lower than that of FNAT-47h (~868 MPa), probably owing to the absence of bcc phase in FNAT-4h. However, the major difference between FNAT-4h and FNAT-47h is in their plastic deformation behaviour. FNAT-4h does not exhibit a sharp increase in WHR upon straining; rather, there are two small humps in the WHR plot of FNAT-4h (Fig. 3c). Neutron diffraction spectra after interrupted tensile tests (corresponding to true strains of 5% and 23%) are shown in Fig. 3e. Before loading, the spectrum ('Initial') contains only fcc and L1<sub>2</sub> peaks. After ~5% true strain, there is no evidence of a bcc peak, indicating that the martensitic transformation does not occur during the first WHR hump. However, the intensity ratio of the fcc (111) peak to the fcc (200) peak increases, consistent with {111} slip-induced texture. At ~23% true strain, a small bcc (110) peak becomes noticeable, suggesting that the second hump corresponds to the transformation from fcc to bcc. Throughout, the intensity ratio of fcc (111) to fcc (200) continues to increase. Together, these results show that the finer, more closely spaced nanoprecipitates in FNAT-4h hinder the formation of not only thermal martensite (during quenching) but also deformation-induced martensite (during tensile testing). By contrast, the coarser and more widely spaced precipitates in FNAT-47h hinder

only thermal martensite but allow deformation-induced martensite to form.

The martensitic transformation in FNAT-47h produces a degree of work hardening ( $\sigma_{UTS}$  (1,830 MPa) –  $\sigma_y$  (868 MPa) = 962 MPa) that is double that reported<sup>9</sup> for a (FeCoNi)<sub>86</sub>Al<sub>7</sub>Ti<sub>7</sub> alloy ( $\sigma_{UTS}$  (1,468 MPa) –  $\sigma_y$  (1,028 MPa) = 440 MPa). The latter also contains L1<sub>2</sub> precipitates in a fcc matrix; however, its matrix does not undergo phase transformation<sup>9</sup>. Consequently, our FNAT alloy, with only approximately 24–26 vol% nanoprecipitates in a simple Fe–Ni-based matrix, is able to achieve either 25% higher (47-h anneal) or comparable (4-h anneal) ultimate strength as the (FeCoNi)<sub>86</sub>Al<sub>7</sub>Ti<sub>7</sub> alloy which has more than double the amount (~55 vol%) of nanoprecipitates in a more concentrated FeCoNi-based

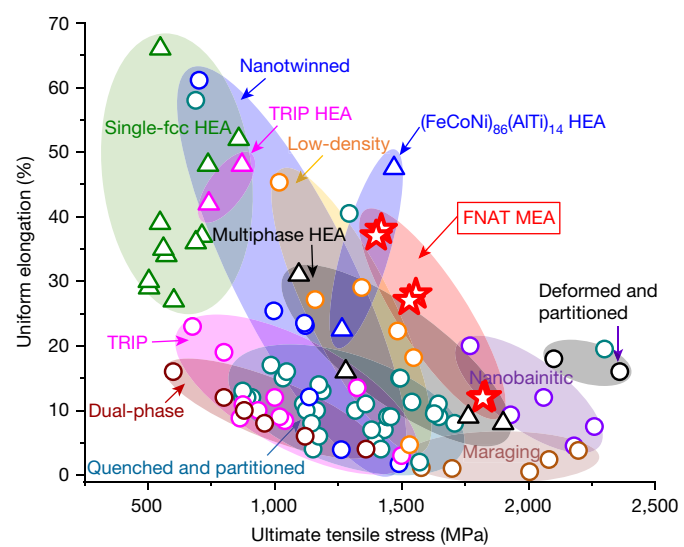


**Fig. 4 | Comparison of uniform elongation versus ultimate tensile strength at room temperature of the current MEAs (FNAT-47h, FNAT-8h, and FNAT-4h) with other HEAs and steels.** The present work is indicated by red stars. The data sources of the different materials are provided in Methods section 'Tensile testing and mechanical properties'.

- matrix. Compared to state-of-the-art high-entropy alloys (HEAs) and steels, the tensile properties of the current FNAT-47h and FNAT-4h MEAs lie at the upper bound, see Fig. 4.
- It is worth noting that we used precipitate characteristics (size and spacing) in this study to control spatial confinement and, in turn, conventional strengthening, martensitic phase transformation, and transformation-induced plasticity, which differs from prior work<sup>21,22</sup> where precipitates were used to alter the matrix composition (and hence the  $M_s$  temperature or stacking fault energy). Our findings illuminate new pathways to optimize the sequential activation of different deformation mechanisms by tuning the characteristics (size, spacing) of dual-function precipitates without changing the alloy composition. Obviously, we can also modify the composition of the matrix to alter the chemical driving force for martensite formation and/or the volume fraction of precipitates to change the spatial confinement effects on strength and phase transformation. We expect the strategy demonstrated here to be applicable to other systems (both conventional alloys and HEAs) that share common features with FNAT, especially the ability to form nanoprecipitates in a phase-transformable matrix (fcc to bcc as in the present case, or fcc to hcp in other cases).
- ## Online content
- Any methods, additional references, Nature Research reporting summaries, source data, extended data, supplementary information, acknowledgements, peer review information; details of author contributions and competing interests; and statements of data and code availability are available at <https://doi.org/10.1038/s41586-021-03607-y>.
1. Gali, A. & George, E. P. Tensile properties of high- and medium-entropy alloys. *Intermetallics* **39**, 74–78 (2013).
  2. Gludovatz, B. et al. Exceptional damage-tolerance of a medium-entropy alloy CrCoNi at cryogenic temperatures. *Nat. Commun.* **7**, 10602 (2016).
  3. Gludovatz, B. et al. A fracture-resistant high-entropy alloy for cryogenic applications. *Science* **345**, 1153–1158 (2014).
  4. Kumar, K., Van Swygenhoven, H. & Suresh, S. Mechanical behavior of nanocrystalline metals and alloys. *Acta Mater.* **51**, 5743–5774 (2003).
  5. Lu, L., Chen, X., Huang, X. & Lu, K. Revealing the maximum strength in nanotwinned copper. *Science* **323**, 607–610 (2009).
  6. Labusch, R. A statistical theory of solid solution hardening. *Phys. Status Solidi B* **41**, 659–669 (1970).
  7. Gladman, T. Precipitation hardening in metals. *Mater. Sci. Technol.* **15**, 30–36 (1999).
  8. Jiang, S. et al. Ultrastrong steel via minimal lattice misfit and high-density nanoprecipitation. *Nature* **544**, 460 (2017).
  9. Yang, T. et al. Multicomponent intermetallic nanoparticles and superb mechanical behaviors of complex alloys. *Science* **362**, 933–937 (2018).
  10. He, B. et al. High dislocation density-induced large ductility in deformed and partitioned steels. *Science* **357**, 1029–1032 (2017).
  11. Lu, K., Lu, L. & Suresh, S. Strengthening materials by engineering coherent internal boundaries at the nanoscale. *Science* **324**, 349–352 (2009).
  12. La Roca, P., Baruj, A., Sobrero, C. E., Malarria, J. A. & Sade, M. Nanoprecipitation effects on phase stability of Fe-Mn-Al-Ni alloys. *J. Alloys Compd.* **708**, 422–427 (2017).
  13. Luo, H., Shan, F., Huo, Y. & Wang, Y. Effect of precipitates on phase transformation behavior of Ti-49 at.% Ni film. *Thin Solid Films* **339**, 305–308 (1999).
  14. Kaufman, L. & Cohen, M. The martensitic transformation in the iron-nickel system. *JOM* **8**, 1393–1401 (1956).
  15. Liang, Y.-J. et al. High-content ductile coherent nanoprecipitates achieve ultrastrong high-entropy alloys. *Nat. Commun.* **9**, 4063 (2018).
  16. Raabe, D., Ponge, D., Dmitrieva, O. & Sander, B. Nanoprecipitate-hardened 1.5 GPa steels with unexpected high ductility. *Scr. Mater.* **60**, 1141–1144 (2009).
  17. Nishiyama, Z. X-ray investigation of the mechanism of the transformation from face centered cubic lattice to body centered cubic. *Sci. Rep. Tohoku Univ.* **23**, 637 (1934).
  18. Fisher, J., Hollomon, J. & Turnbull, D. Kinetics of the austenite → martensite transformation. *Metals Trans.* **18S**, 691–700 (1949).
  19. Jimenez-Melero, E. et al. Martensitic transformation of individual grains in low-alloyed TRIP steels. *Scr. Mater.* **56**, 421–424 (2007).
  20. Yang, H.-S. & Bhadeshia, H. Austenite grain size and the martensite-start temperature. *Scr. Mater.* **60**, 493–495 (2009).
  21. Jin, S., Morris, J., Chen, Y., Thomas, G. & Jaffee, R. An investigation of transformation strengthening in precipitation-hardened Fe-Ni austenite. *Metall. Trans. A* **9**, 1625–1633 (1978).
  22. Wang, T. et al. Co-introduction of precipitate hardening and TRIP in a TWIP high-entropy alloy using friction stir alloying. *Sci. Rep.* **11**, 1–10 (2021).

**Publisher's note** Springer Nature remains neutral with regard to jurisdictional claims in published maps and institutional affiliations.

© The Author(s), under exclusive licence to Springer Nature Limited 2021

## Methods

### Alloy design

The FNAT alloy was designed following the CALPHAD approach<sup>23</sup>; calculations of phase equilibria were performed with Pandat ([www.compuTherm.com](http://www.compuTherm.com))<sup>24</sup>. Three main criteria were considered in the alloy design process. First, the alloy needs to have a fcc matrix containing 20 to 30 mol% of ductile L1<sub>2</sub> precipitates for strengthening. Second, the alloy should contain only L1<sub>2</sub> precipitates and not any potentially embrittling intermetallics. Third, the matrix composition should be such that, when cooled quickly to room temperature, it should undergo a transformation to bcc-martensite. Based on these, a composition of Fe-32.6Ni-6.1Al-2.9Ti (at%) was selected. Besides the major elements, small amounts of 0.1Zr, 0.2C and 0.03B (at%) were added for grain refinement; they were assumed to have a negligible effect on phase equilibria. The chemical composition after melting and casting (see process steps below) was analysed by Luvak Laboratories and found to be Fe-31.7Ni-6.0Al-3.0Ti-0.1Zr-0.2C-0.02B (at%) which is close to its thermodynamically targeted composition. For comparison with the above two-phase alloy, another alloy designated as FNAT-m (having the composition Fe-23Ni-3.6Al-0.5Ti, at%) of the matrix of the FNAT alloy, along with 0.1Zr, 0.2C and 0.03B (at%), was also produced and processed identically to the FNAT alloy (details below).

We refer to FNAT as a medium-entropy alloy after Yeh et al.<sup>25</sup> who classified near-equiatomic alloys containing 2–4 elements as medium-entropy alloys and those with 5 or more elements as high-entropy alloys. Alternatively, these criteria can be expressed in terms of the ideal configurational mixing entropy, which for medium-entropy alloys is 5.76 to 11.52 J mol<sup>-1</sup> K<sup>-1</sup>. Our FNAT alloy has ideal configurational mixing entropies of 7.92 J mol<sup>-1</sup> K<sup>-1</sup> if we consider its bulk composition (Fe-32.6Ni-6.1Al-2.9Ti, at%) and 5.92 J mol<sup>-1</sup> K<sup>-1</sup> if we consider just its matrix composition (Fe-23Ni-3.6Al-0.5Ti, at%), both of which fall within the range given by Yeh et al.<sup>25</sup> for medium-entropy alloys.

The calculated equilibrium phases and their amounts in the FNAT alloy are plotted in Extended Data Fig. 1a for temperatures in the range 300–1,600 °C. It shows that the alloy is single-phase fcc between 925 °C and 1,240 °C. At 925 °C and below, L1<sub>2</sub> precipitates form in the fcc matrix. Based on the predicted phase equilibria, we chose a solutionizing temperature of 1,100 °C and an ageing temperature of 700 °C to form a two-phase mixture of L1<sub>2</sub> nanoprecipitates in a fcc matrix. The calculated phase equilibria also show the amount of L1<sub>2</sub>(Ni,Fe)<sub>3</sub>(Al,Ti) precipitates as ~25 mol% at 700 °C. The selected composition thus satisfies the first two design criteria mentioned earlier.

After element partitioning during the formation of precipitates, the concentrations of Ni, Al and Ti in the fcc matrix are reduced to ~23 at%, ~3.5 at% and ~0.5 at%, respectively (Extended Data Fig. 1b). This fcc matrix is predicted to transform to the equilibrium bcc ferrite phase (bcc\_eq, denoted by the dashed line in Extended Data Fig. 1a) at temperatures of ~625 °C and below. However, for this transformation to occur, long-range diffusion is required to transfer Ni from fcc to bcc\_eq as the Ni content in these two phases is very different; for example, the maximum solubility of Ni in bcc\_eq is ~5 at%<sup>26</sup> whereas the Ni content in the fcc matrix is ~23 at%. Owing to sluggish diffusion kinetics at 625 °C and below<sup>27</sup>, we were able to prevent this transformation by using a cooling rate (water quenching) that was fast enough to preclude long-range diffusion.

Although a diffusion-controlled fcc-to-bcc\_eq transition cannot occur, our first principles calculations (see below) show that for the matrix composition Fe-23Ni-3.6Al-0.5Ti (at%) at temperatures lower than 500 °C, the bcc structure is more stable than the fcc structure, suggesting a thermodynamic driving force is available for the diffusion-less fcc → bcc transition (Extended Data Fig. 1c). Note that the ‘bcc’ here is different to ‘bcc\_eq’ as the former retains the same composition as the parent fcc phase. This driving force originates from the change in

magnetic state from paramagnetic (fcc) to ferromagnetic (bcc), which may explain why martensitic transformation, a known diffusionless phase transition, can occur in Fe–Ni alloys during quenching. Despite this thermodynamic driving force, a kinetic energy barrier has to be overcome for martensitic transformation to occur<sup>28</sup>. Therefore, the martensite start temperature ( $M_s$ ) requires undercooling below  $T_0$ , the temperature at which the free energy curves of the fcc and bcc phases cross in Extended Data Fig. 1c. The reported  $M_s$  temperatures of Fe-22–24 at% Ni alloys are around 200 °C, with a martensite finish ( $M_f$ ) temperature above 25 °C<sup>14</sup>. Assuming negligible effects of Al and Ti on the martensitic transformation (given their small concentrations), the fcc matrix (Fe-23 at% Ni) in the FNAT alloy should completely transform to martensite if we quench it into a room-temperature (~21 °C) water bath. This satisfied the third design criterion.

### Alloy fabrication and sample preparation

Alloy buttons, each weighing ~150 g, were prepared from the constituent elements (purity >99.95 at%) by arc melting in an Ar atmosphere on a water-chilled copper hearth. Before the alloys were melted, the furnace chamber was evacuated, flushed and backfilled with high-purity Ar gas, and a small piece of Ti was melted to getter any residual oxygen and nitrogen. The alloy buttons were flipped and remelted 10 times to ensure good homogeneity and drop-cast into a copper mould with dimensions of 12.7 mm × 12.7 mm × 76.2 mm. The total weight loss after casting was less than 0.1%, which explains the closeness between the analysed and target compositions. Ingots were homogenized at 1,100 °C for 2 h, followed by hot rolling at ~1,100 °C to produce a 70% reduction in thickness. Subsequently, solutionizing was performed at 1,100 °C for 30 min, followed by quenching in a room-temperature water bath. The quenched sheets were cut into ~10 cm × 1.5 cm × 0.37 cm pieces, some of which were then aged at 700 °C for 47 h, 8 h or 4 h to form L1<sub>2</sub> precipitates and quenched into a room-temperature water bath, whereas the others were spared the ageing treatment to enable investigation of the as-solutionized state. All heat treatments were conducted in air.

### Tensile testing and mechanical properties

Flat dog-bone-shaped tensile specimens with a gauge length of 12.7 mm were machined after the heat treatments by electro-discharge machining with their longitudinal axes parallel to the rolling direction, and ground with 600 grit SiC abrasive papers. Tensile tests were performed at room temperature in air using an MTS servo-hydraulic test rig at a nominal engineering strain rate of 10<sup>-3</sup> s<sup>-1</sup>. The strength and ductility reported here are averages from four tensile tests. Loads were measured with a calibrated load cell from which engineering stresses were calculated using the initial cross-sectional areas. Engineering strains were determined using non-contact optical displacement/strain measurement method, that is, 2D Digital Image Correlation. A random black and white speckle pattern was created on the specimen surface using Rust-Oleum primer and Ceylon ultra-flat black spray paints. These speckle patterns provide the reference for digital image correlation (DIC) processing. During the tensile tests, sequential images are recorded using a GS3-U3-51S5M-C 2/3" FLIR Grasshopper3 High Performance USB 3.0 Monochrome Camera with 50 mm C Series fixed-focal-length lens. The images are post-processed to form deformation contours based on a pattern-matching algorithm using the commercial software VIC-2D Version 6.0.2 (Correlated Solutions). This algorithm uses subset-based normalized cross-correlation criteria by comparing the reference subset in subsequent images. The engineering strains are exported from each image using an inspection extensometer on the strain map. The standard deviation of the strain values obtained using this setup is ±0.0005. Yield strengths were measured by the usual 0.2% offset method.

An approximate yield strength of the FNAT alloys can be estimated by simply summing the volume-fraction-weighted contributions to

strength from each phase (retained austenite, bcc martensite, and the L<sub>1</sub><sub>2</sub> precipitates in the fcc and bcc matrices) as follows:

$$\sigma_{FNAT} = f_{fcc} (\sigma_{fcc} + \Delta\sigma_{fcc}) + f_{bcc} (\sigma_{bcc} + \Delta\sigma_{bcc}), \quad (1)$$

where  $f_{fcc}$ ,  $\sigma_{fcc}$ , and  $f_{bcc}$ ,  $\sigma_{bcc}$ , are the respective volume fractions and yield strengths of the fcc and bcc matrices, and  $\Delta\sigma_{fcc}$  and  $\Delta\sigma_{bcc}$  are the respective increases of the yield strengths of the fcc and bcc matrices due to the L<sub>1</sub><sub>2</sub> precipitates. The volume fraction of the bcc phase ( $f_{bcc}$ ) is 0.06 and its yield strength ( $\sigma_{bcc}$ ) was approximated by the measured yield strength of FNAT-m-47h (~705 MPa) after water quenching, as it was almost fully martensitic and did not contain any nanoprecipitates (Fig. 1i). The volume fraction of the fcc phase ( $f_{fcc}$ ) is 0.94 and to obtain its yield strength ( $\sigma_{fcc}$ ) we performed a tensile test on the FNAT alloy in the solutionized state, see Extended Data Fig. 2a, from which the yield strength was estimated as ~325 MPa.

The strengthening arising from dislocation cutting of the L<sub>1</sub><sub>2</sub> precipitates in the fcc and bcc regions (confirmed in Extended Data Fig. 2b-c) was estimated using the following expression<sup>29</sup>:

$$\Delta\sigma = 0.81M \left( \frac{\gamma_{APB}}{2b} \right) \left( \frac{3\pi f}{8} \right)^{\frac{1}{2}}, \quad (2)$$

where  $M$  in the above expression is the Taylor factor and the Burgers vector,  $b$ , is  $\frac{1}{2}\langle 110 \rangle$  for fcc and  $\frac{1}{2}\langle 111 \rangle$  for bcc. The lattice parameters for fcc (0.359 nm) and bcc (0.287 nm) were obtained from neutron diffraction.  $\gamma_{APB}$  is the antiphase boundary energy, which has been extensively studied for Ni<sub>3</sub>Al {111}. The various reported values were reviewed and compared with results of ab initio calculations in the literature<sup>30</sup> and found to lie primarily between 175–225 mJ m<sup>-2</sup>. In this work, it was taken as  $200 \pm 25$  mJ m<sup>-2</sup> for the L<sub>1</sub><sub>2</sub> precipitates in both fcc and bcc matrices. Given experimental uncertainties we consider the volume fraction of precipitates to be an average (0.26) of those obtained from the three different techniques, neutron diffraction (0.28), APT (0.26) and SANS (0.24) in both fcc and bcc matrices. The Taylor factor  $M$  and Burgers vector  $b$  for the fcc matrix are 3.06 (ref. <sup>9</sup>) and 0.254 nm (from our measured lattice parameter), respectively. The Taylor factor  $M$  and Burgers vector  $b$  for the bcc matrix are 2.73 (ref. <sup>31</sup>) and 0.248 nm (from our measured lattice parameter), respectively. Using these parameters and equation (2), the strengthening contribution can be estimated as 811 MPa in the fcc regions and 72 MPa in the bcc regions. Finally, using equation (1), the yield strength of the FNAT alloy can be estimated as  $883 \pm 67$  MPa (where the error is from the uncertainty in  $\gamma_{APB}$ ), which is comparable to the experimentally measured value of  $862 \pm 6$  MPa. A large portion,  $535 \pm 67$  MPa (where the error is from the uncertainty in  $\gamma_{APB}$ ), of the estimated yield strength of FNAT is due to the total strengthening from nanoprecipitates in the fcc and bcc regions.

True stress ( $\sigma_t$ ) and true strain ( $\epsilon_t$ ) were calculated from engineering stress ( $\sigma_e$ ) and engineering strain ( $\epsilon_e$ ) using the well known equations:

$$\sigma_t = \sigma_e (1 + \epsilon_e), \quad (3)$$

$$\epsilon_t = \ln(1 + \epsilon_e). \quad (4)$$

The tensile properties of the current FNAT-47h and FNAT-4h MEAs are compared to those of state-of-the-art HEAs and steels in Fig. 4. The different materials plotted and their data sources are transformation-induced plasticity (TRIP) steel<sup>16,32,33</sup>, dual-phase steel<sup>34</sup>, maraging steel<sup>18,35,36</sup>, nanobainitic steel<sup>37</sup>, low-density steel<sup>38</sup>, quenched and partitioned steel<sup>39,40</sup>, nanotwin steel<sup>41,42</sup>, deformed and partitioned steel<sup>10</sup>, single-phase fcc HEAs<sup>3,43,44</sup>, multiphase HEAs<sup>15,45</sup>, TRIP HEAs<sup>46</sup>, and (FeCoNi)<sub>86</sub>(AlTi)<sub>14</sub> HEAs containing single-function nanoprecipitates<sup>9</sup>.

We also measured the tensile properties of FNAT-47h at 700 °C. Because of the difficulty in using DIC at elevated temperatures, strain

could only be estimated from crosshead displacement, which makes it unreliable and is therefore not presented. However, loads can be measured accurately, which makes the ultimate tensile stress (UTS) reliable. Therefore, we have compared the UTS of FNAT-47h at 700 °C with those of other Ni- and Fe-based high-temperature alloys in Extended Data Fig. 5.

## TEM/STEM

TEM samples were lifted out using a FEI Versa 3D FIB/SEM dual-beam system. The lamellae were thinned with a 30 kV Ga beam to about 200 nm and then polished at progressively lower voltages (8, 5 and 2 kV) to gradually reduce the sample thickness to about 50 nm. JEOL JEM 2100F was used for general TEM/STEM imaging at 200 kV. High-angle annular dark-field STEM with Z-contrast imaging was performed using an aberration-corrected Nion UltraSTEM operated at 200 kV. In that mode, the bright spots correspond to atomic columns with the intensity depending on the atomic number ( $Z$ ) and the number of atoms in the column. For example, Ni-rich columns appear brighter than Al-rich columns; the overall intensity depends on the sample thickness.

## EBSD

Samples were mechanically polished to a mirror finish using conventional metallographic sample preparation steps. The two final polishing steps were electropolishing in an electrolyte (85% H<sub>3</sub>PO<sub>4</sub> solution) at 6 V and 2 A for 10 min at room temperature, followed by ion-milling at 2 kV for 20 min. Scanning electron microscopy (SEM) characterization was carried out using a JEOL 6500 SEM equipped with an EDAX EBSD system. EBSD mapping was conducted at 20 kV on  $400 \times 200 \mu\text{m}^2$  or larger areas with a step size of 0.35  $\mu\text{m}$ .

EBSD was also used to evaluate texture after hot-rolling and annealing. The pole figures of FNAT-47h and FNAT-m-47h calculated by the harmonic series expansion method with 5° Gaussian smoothing using the TSL OIM analysis software are shown in Extended Data Fig. 6a, b and Extended Data Fig. 6c, d, respectively. In addition, on the basis of images such as those shown in Fig. 1e–g, we measured the prior austenite grain size to be  $36 \pm 9 \mu\text{m}$  in both FNAT-47h and FNAT-m-47h.

## Neutron diffraction

Neutron diffraction was conducted on the engineering materials diffractometer, VULCAN, at the Spallation Neutron Source, Oak Ridge National Laboratory. A high-resolution neutron diffraction mode with  $d$ -spacing coverage of 0.5–3.5 Å was used and Rietveld refinement was performed using GSAS with EXPGUI. FNAT-47h samples tensile tested to true strains of 2% and 8%, FNAT-4h samples tensile tested to 5% and 23% true strains, as well as their initial state before tensile testing (0% strain) were subjected to neutron diffraction. The fcc, bcc and L<sub>1</sub><sub>2</sub> structures were used to refine the phase fraction, lattice misfit, and so on. Lattice parameters of L<sub>1</sub><sub>2</sub>, bcc and fcc were determined to be 0.3590, 0.2866 and 0.3593 nm, respectively. In addition to phase analysis, neutron diffraction was also used to evaluate texture of FNAT-47h after hot-rolling and annealing. The two spectra in Extended Data Fig. 6e were obtained from two different detector banks that measure the diffraction along the rolling direction (RD) and the normal direction (ND). The RD and ND spectra have been slightly shifted horizontally with respect to each other to facilitate comparison (otherwise the peaks would overlap).

## SANS

Spectra were collected on the CG2 General-Purpose SANS at HFIR<sup>47</sup> using three instrument settings, spanning a total  $Q$  range of 0.0007 to  $1 \text{ \AA}^{-1}$ : a sample-detector distance of 19.2 m using 12 Å neutrons to measure the lowest  $Q$  and largest scattering objects, a sample-detector distance of 7.0 m using 4.75 Å neutrons to measure the middle of the range, and a sample-detector distance of 1.0 m using 4.75 Å neutrons to measure the highest  $Q$  and the smallest scattering objects. The data were reduced using software routines written by the instrument scientist according

# Article

to standard procedures and were placed on an absolute scale using an attenuated direct beam.

The SANS data were fitted to polydisperse spheres, spheres, and ellipses. The calculated scattering length density using the APT-measured precipitate composition as input is  $-1.40 \times 10^{-6} \text{ cm}^{-2}$ . The precipitate parameters were calculated from different fits (Extended Data Table 1). Although there are differences, the SANS data that were modelled as polydisperse spheres with a Schultz hard-sphere interaction potential<sup>48</sup> assuming smooth boundary interfaces are in very good agreement with the APT results, given the limitations of the respective techniques.

## APT

A FEI Nova 200 dual-beam focused-ion-beam (FIB) instrument was used to perform site-specific lift-outs from specimen regions of interest in the same sample as that used for SEM and to perform annular milling to fabricate the needle-shaped APT specimens. A wedge lift-out geometry was used to mount multiple samples on a Si microtip coupon to enable the fabrication of multiple APT needles from one wedge lift-out<sup>49</sup>. A final 2 kV polishing step was used to minimize Ga implantation damage and to sharpen the APT needle within the specific region of interest. The APT data were acquired using a local electrode atom probe (CAMECA Instruments LEAP 4000X HR) equipped with an energy-compensated reflection lens and a 36% detection efficiency. The APT experiments were conducted at a specimen base temperature of 30 K by applying 60–85 pJ, 355 nm wavelength, 10 ps laser pulses at a repetition rate of 100 kHz and a detection rate of 0.5% to 1.0%. The laser energy was chosen to keep an  $\text{Fe}^{++}/\text{Fe}^+$   $m/q$  peak ratio of approximately 10. Data reconstruction and analyses were performed using CAMECA IVAS 3.8 software. Precipitate parameters were calculated using 40 at%, 50 at%, and 60 at% Ni iso-concentration surfaces. The results are shown in Extended Data Table 2. A 60 at% iso-concentration surface showed the best agreement with the neutron diffraction data.

## First-principles calculations

The electronic structures of the fcc and bcc matrices were calculated by applying the coherent potential approximation (CPA)<sup>50,51</sup> and multiple scattering theory formalism<sup>52</sup> as implemented in the CPA SPR-KKR method<sup>53</sup>. The exchange-correlation energy was calculated using the parametrization by Perdew et al.<sup>54</sup> The phonon part of the free energy is calculated using a combination of the Phonopy<sup>55</sup> and Quantum Espresso<sup>56</sup> packages. The magnetic states of the  $\text{L1}_2$  precipitate, the fcc matrix, and the bcc matrix at different temperatures were investigated to determine their magnetic free energy.

Magnetic ordering in the matrix composition of the FNAT alloy was described by the classical Heisenberg model:

$$\hat{H} = - \sum_{i,j; i \neq j} J_{ij} \mathbf{e}_i \cdot \mathbf{e}_j, \quad (5)$$

where  $\mathbf{e}_i$  and  $\mathbf{e}_j$  are the direction of the magnetic moment of atoms  $i$  and  $j$ ,  $J_{ij}$  are the exchange coupling parameters. The values for  $J_{ij}$  are calculated using a linear response approach<sup>57</sup>. The averaged magnetic moments of the alloy phases as a function of temperature are calculated using the cluster field method<sup>58,59</sup>. The Curie temperatures were determined for the precipitate,  $T_c = 75$  K, the fcc phase,  $T_c \approx 1,000$  K, and the bcc phase,  $T_c \approx 1,500$  K. The Curie temperature for the fcc matrix is overestimated by ~170 K compared to experimental data<sup>60</sup>, which is probably because of the rigid treatment of the magnetic moment of the Ni atoms in equation (5). Therefore, at our ageing temperature (973 K), the precipitates and the fcc matrix should be in a paramagnetic state whereas the bcc phase is ordered ferromagnetically. The paramagnet is approximated by a disordered local magnetic moment (DLM) approximation<sup>61</sup>. The calculated interplanar spacings were:  $d\{111\}_{\text{L1}_2} = 0.2074 \text{ nm}$ ,  $d\{111\}_{\text{fcc}} = 0.20716 \text{ nm}$ , and  $d\{111\}_{\text{bcc}} = 0.2037 \text{ nm}$ . With these values, the lattice misfit between  $\text{L1}_2$  and fcc matrix is 0.1%, and that between  $\text{L1}_2$  and bcc

matrix is 1.7%. The misfit is defined as  $(d_{\text{ppt}} - d_{\text{matrix}})/d_{\text{matrix}}$ . The  $\text{L1}_2$ –fcc misfit is identical to the experimentally measured misfit whereas the  $\text{L1}_2$ –bcc misfit is lower than the experimental value of 2.2%. A possible reason for this difference is that the magnetic moment in bcc phase is partially disordered at the annealing temperature, whereas we calculated its lattice parameter in the perfectly ordered ferromagnetic state.

The equations of state for both structures were calculated in ferromagnetic and DLM magnetic states to demonstrate the magnetic origin of the fcc–bcc transition and to obtain a reference point for elastic contribution to free energy. In this approach, the DLM state corresponds to a high-temperature state (above the Curie temperature), and the ferromagnetic state corresponds to a low-temperature state. To calculate the structural transition temperature ( $T_0$ ), the additional phonon contribution,  $F_{\text{phon}}$ , to free energy together with elastic energy,  $E_{\text{elas}}$ , should be included:

$$F(T) = E_{\text{elas}} + F_{\text{mag}}(T) + F_{\text{phon}}(T), \quad (6)$$

where  $F_{\text{mag}}$  is the magnetic part of the free energy.

The phonon part of the free energy was calculated using the following standard expression:

$$F_{\text{phon}}(T) = -k_B T \int_0^\infty d\omega N(\omega) \ln \left( 1 - e^{-\frac{\omega}{k_B T}} \right), \quad (7)$$

where the phonon density of states  $N(\omega)$  is calculated using a combination of the Phonopy<sup>55</sup> and Quantum Espresso<sup>56</sup> packages. The calculation was carried out using a plane-wave basis set and ultrasoft pseudopotentials optimized in the RRKJ scheme<sup>62</sup>. With an almost negligible amount of aluminium in both the fcc and bcc structures, the alloys were treated as a binary  $\text{Ni}_{0.2}\text{Fe}_{0.79}$  alloy (modelled using virtual crystal approximation, VCA)<sup>63</sup>. As a realization of the VCA for the pseudopotential method, we used the scheme proposed by Ramer and Rappe<sup>63</sup>. Similar to pure iron, ferromagnetic fcc  $\text{Ni}_{0.2}\text{Fe}_{0.79}$  is dynamically unstable, and the antiferromagnetic [111] state was used to model the stable high-temperature paramagnetic state. The transition temperature ( $T_0$ ) was calculated to be approximately 770 K when the phonon contribution was incorporated into the analysis of the magnetic part of the free energy of the system. The transition is of the first order, as shown in Extended Data Fig. 1c, and is accompanied by a step-like change of magnetization.

## Fracture behaviour

The fracture behaviour of FNAT-47h and FNAT-m-47h were analysed with SEM and DIC strain maps. The FNAT-m-47h alloy (which is almost fully martensitic before tensile testing and contains no precipitates) shows considerable necking before fracture and exhibited strain localization (Extended Data Fig. 7a) in the region where fracture eventually occurs. By contrast, the FNAT-47 alloy, which contains ~26 vol% precipitates and undergoes martensitic transformations during tensile testing, showed minimal necking near the fracture surface, and the DIC strain maps show that strain is distributed relatively diffusely throughout the gage section with no evidence of localization near the fracture plane (Extended Data Fig. 7b).

## Data availability

All figures have associated raw data, available on request from Y.Y.

23. Kaufman, L. & Bernstein, H. *Computer Calculation of Phase Diagrams. With Special Reference to Refractory Metals* (Academic Press, 1970).
24. Cao, W. et al. PANDAT software with PanEngine, PanOptimizer and PanPrecipitation for multi-component phase diagram calculation and materials property simulation. *Calphad* **33**, 328–342 (2009).
25. Yeh, J. W., Chen, Y. L., Lin, S. J. & Chen, S. K. in *Materials Science Forum* Vol. 560 (eds Balmori-Ramirez, H. et al.) 1–9 (Trans Tech Publ, 2007).

26. Cacciamani, G. et al. Critical evaluation of the Fe–Ni, Fe–Ti and Fe–Ni–Ti alloy systems. *Intermetallics* **14**, 1312–1325 (2006).
27. Borgenstam, A. & Hillert, M. Massive transformation in the Fe–Ni system. *Acta Mater.* **48**, 2765–2775 (2000).
28. Nishiyama, Z. *Martensitic Transformation* (Elsevier, 2012).
29. Ardell, A. J. Precipitation hardening. *Metall. Trans. A* **16**, 2131–2165 (1985).
30. Gorbatov, O. I. et al. Effect of composition on antiphase boundary energy in Ni<sub>3</sub>Al-based alloys: ab initio calculations. *Phys. Rev. B* **93**, 224106 (2016).
31. Rosenberg, J. & Piehler, H. Calculation of the Taylor factor and lattice rotations for bcc metals deforming by pencil glide. *Metall. Trans. A* **2**, 257–259 (1971).
32. Zhang, M., Li, L., Fu, R., Krizan, D. & De Cooman, B. Continuous cooling transformation diagrams and properties of micro-alloyed TRIP steels. *Mater. Sci. Eng. A* **438–440**, 296–299 (2006).
33. Zhao, J.-L., Yan, X., Wen, S. & Lin, L. Microstructure and mechanical properties of high manganese TRIP steel. *J. Iron Steel Res. Int.* **19**, 57–62 (2012).
34. Bouaziz, O., Zuorob, H. & Huang, M. Driving force and logic of development of advanced high strength steels for automotive applications. *Steel Res. Int.* **84**, 937–947 (2013).
35. Boyer, H. E. *Atlas of Stress–Strain Curves* (ASM International, 1987).
36. Morris, J., Jr. Maraging steels: Making steel strong and cheap. *Nat. Mater.* **16**, 787 (2017).
37. García-Mateo, C. & Caballero, F. G. The role of retained austenite on tensile properties of steels with bainitic microstructures. *Mater. Trans.* **46**, 1839–1846 (2005).
38. Kim, S.-H., Kim, H. & Kim, N. J. Brittle intermetallic compound makes ultrastrong low-density steel with large ductility. *Nature* **518**, 77–79 (2015).
39. De Moor, E., Speer, J. G., Matlock, D. K., Kwak, J.-H. & Lee, S.-B. Effect of carbon and manganese on the quenching and partitioning response of CMnSi steels. *ISIJ Int.* **51**, 137–144 (2011).
40. Dong, X., Shen, Y., Yin, T., Misra, R. & Lin, G. Strengthening a medium-carbon steel to 2800 MPa by tailoring nanosized precipitates and the phase ratio. *Mater. Sci. Eng. A* **759**, 725–735 (2019).
41. Bouaziz, O., Barbier, D., Cugy, P. & Petigand, G. Effect of process parameters on a metallurgical route providing nano-structured single phase steel with high work-hardening. *Adv. Eng. Mater.* **14**, 49–51 (2012).
42. Wang, H., Tao, N. & Lu, K. Strengthening an austenitic Fe–Mn steel using nanotwinned austenitic grains. *Acta Mater.* **60**, 4027–4040 (2012).
43. Otto, F. et al. The influences of temperature and microstructure on the tensile properties of a CoCrFeMnNi high-entropy alloy. *Acta Mater.* **61**, 5743–5755 (2013).
44. Wu, Z., Bei, H., Pharr, G. M. & George, E. P. Temperature dependence of the mechanical properties of equiatomic solid solution alloys with face-centered cubic crystal structures. *Acta Mater.* **81**, 428–441 (2014).
45. He, J. et al. A precipitation-hardened high-entropy alloy with outstanding tensile properties. *Acta Mater.* **102**, 187–196 (2016).
46. Li, Z., Pradeep, K. G., Deng, Y., Raabe, D. & Tasan, C. C. Metastable high-entropy dual-phase alloys overcome the strength–ductility trade-off. *Nature* **534**, 227 (2016).
47. Wignall, G. D. et al. The 40 m general purpose small-angle neutron scattering instrument at Oak Ridge National Laboratory. *J. Appl. Cryst.* **45**, 990–998 (2012).
48. Kotlarchyk, M. & Chen, S. H. Analysis of small angle neutron scattering spectra from polydisperse interacting colloids. *J. Chem. Phys.* **79**, 2461–2469 (1983).
49. Thompson, K. et al. In situ site-specific specimen preparation for atom probe tomography. *Ultramicroscopy* **107**, 131–139 (2007).
50. Soven, P. Coherent-potential model of substitutional disordered alloys. *Phys. Rev.* **156**, 809 (1967).
51. Taylor, D. Vibrational properties of imperfect crystals with large defect concentrations. *Phys. Rev.* **156**, 1017 (1967).
52. Stocks, G., Temmerman, W. & Gyorffy, B. Complete solution of the Korringa–Kohn–Rostoker coherent-potential-approximation equations: Cu–Ni alloys. *Phys. Rev. Lett.* **41**, 339 (1978).
53. Ebert, H., Koederitzsch, D. & Minar, J. Calculating condensed matter properties using the KKR-Green's function method—recent developments and applications. *Rep. Prog. Phys.* **74**, 096501 (2011).
54. Perdew, J. P., Burke, K. & Ernzerhof, M. Generalized gradient approximation made simple. *Phys. Rev. Lett.* **77**, 3865 (1996).
55. Togo, A. & Tanaka, I. First principles phonon calculations in materials science. *Scr. Mater.* **108**, 1–5 (2015).
56. Giannozzi, P. et al. QUANTUM ESPRESSO: a modular and open-source software project for quantum simulations of materials. *J. Phys. Condens. Matter* **21**, 395502 (2009).
57. Liechtenstein, A. I., Katsnelson, M., Antropov, V. & Kubanov, V. Local spin density functional approach to the theory of exchange interactions in ferromagnetic metals and alloys. *J. Magn. Magn. Mater.* **67**, 65–74 (1987).
58. Vaks, V. & Zein, N. Theory of phase transitions in solid solutions. *J. Exp. Theor. Phys.* **40**, 537 (1975).
59. Vaks, V. & Samolyuk, G. On accuracy of different cluster models used in describing ordering phase transitions in fcc alloys. *J. Exp. Theor. Phys.* **88**, 89–100 (1999).
60. Chuang, Y.-Y., Chang, Y. A., Schmid, R. & Lin, J.-C. Magnetic contributions to the thermodynamic functions of alloys and the phase equilibria of Fe–Ni system below 1200 K. *Metall. Trans. A* **17**, 1361–1372 (1986).
61. Edwards, D. The paramagnetic state of itinerant electron systems with local magnetic moments. I. Static properties. *J. Phys. F Met. Phys.* **12**, 1789 (1982).
62. Rappe, A. M., Rabe, K. M., Kaxiras, E. & Joannopoulos, J. Optimized pseudopotentials. *Phys. Rev. B* **41**, 1227 (1990).
63. Ramer, N. J. & Rappe, A. M. Virtual-crystal approximation that works: locating a compositional phase boundary in Pb(Zr<sub>1-x</sub>Ti<sub>x</sub>)O<sub>3</sub>. *Phys. Rev. B* **62**, R743 (2000).
64. Kurdjumov, G. & Sachs, G. Crystallographic orientation relationship between α-and γ-Fe. *Ann. Phys.* **64**, 325 (1930).
65. American Iron and Steel Institute. *High-Temperature Characteristics of Stainless Steel A Designer's Handbook* Report No. 9004 (Nickel Development Institute, 1979); [https://nickelinstitute.org/media/1699/high\\_temperaturecharacteristicsofstainlesssteel\\_9004\\_.pdf](https://nickelinstitute.org/media/1699/high_temperaturecharacteristicsofstainlesssteel_9004_.pdf)
66. Warlimont, H. & Martienssen, W. *Springer Handbook of Materials Data* (Springer, 2018).

**Acknowledgements** This research was supported by the US Department of Energy, Office of Science, Basic Energy Sciences, Materials Sciences and Engineering Division (testing and analysis of mechanical properties and responsible deformation mechanisms, TEM characterization of the FNAT-4h alloy, and writing of the manuscript) and by the Laboratory Directed Research and Development programme of Oak Ridge National Laboratory (ORNL) (microstructural characterization and first-principles calculations), managed by UT-Battelle, LLC, for the US Department of Energy. YY. acknowledges CompuTherm for providing the phase diagram calculation software Pandat. Resources at ORNL's High Flux Isotope Reactor for small-angle neutron scattering, Spallation Neutron Source for neutron diffraction, and Center for Nanophase Materials Sciences for atom probe tomography were used in this study, which are US DOE Office of Science User Facilities.

**Author contributions** YY. conceived the study, designed the alloy and supervised the project. T.C., A.R.L., A.B. and L.T. performed the TEM and STEM analyses. L.T. performed EBSD analysis. K.A. performed neutron diffraction and phase analysis. Y.W. performed and analysed tensile tests with DIC. J.D.P. performed the APT analysis. G.D.S. performed the first-principles calculations. K.L. performed the SANS analysis. YY. and E.P.G. analysed and interpreted the mechanical properties and deformation mechanisms and wrote the manuscript. All authors reviewed and commented on the manuscript.

**Competing interests** The authors declare no competing interests.

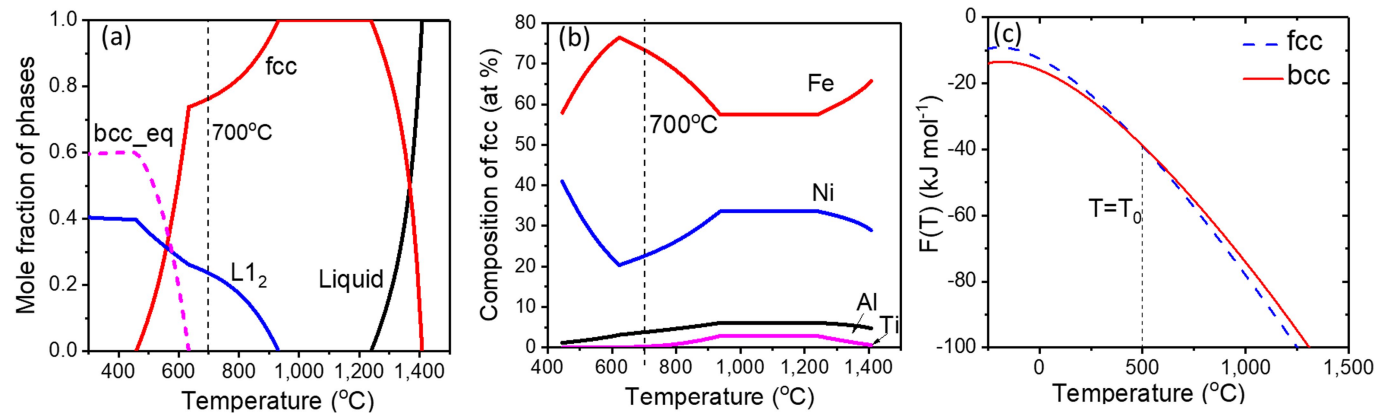
#### Additional information

**Correspondence** and requests for materials should be addressed to Y.Y. or E.P.G.

**Peer review information** *Nature* thanks the anonymous reviewers for their contribution to the peer review of this work.

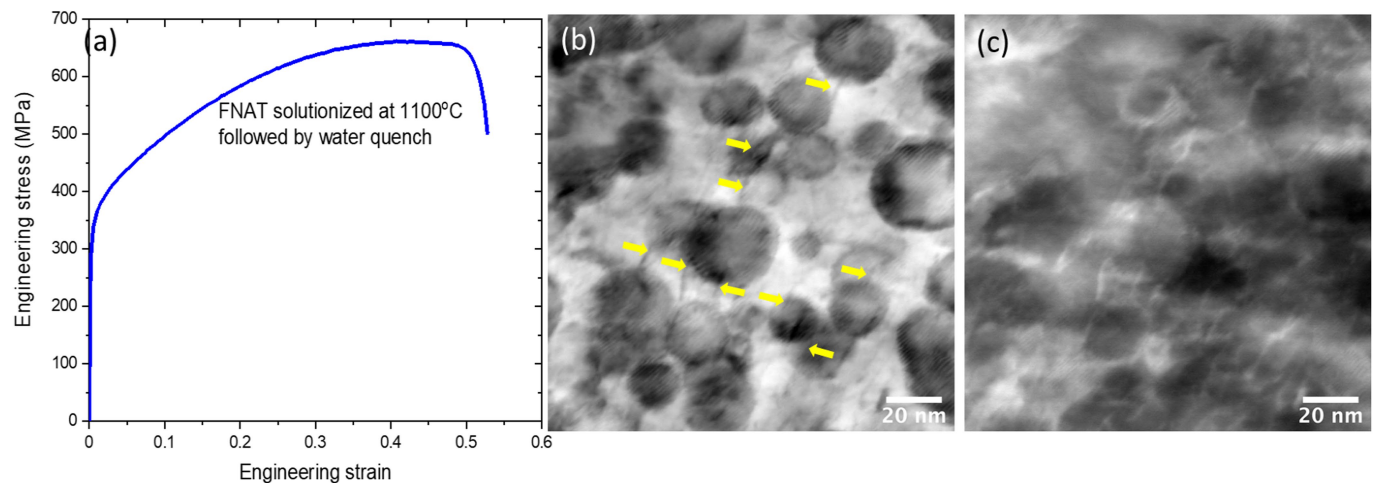
**Reprints and permissions information** is available at <http://www.nature.com/reprints>.

# Article



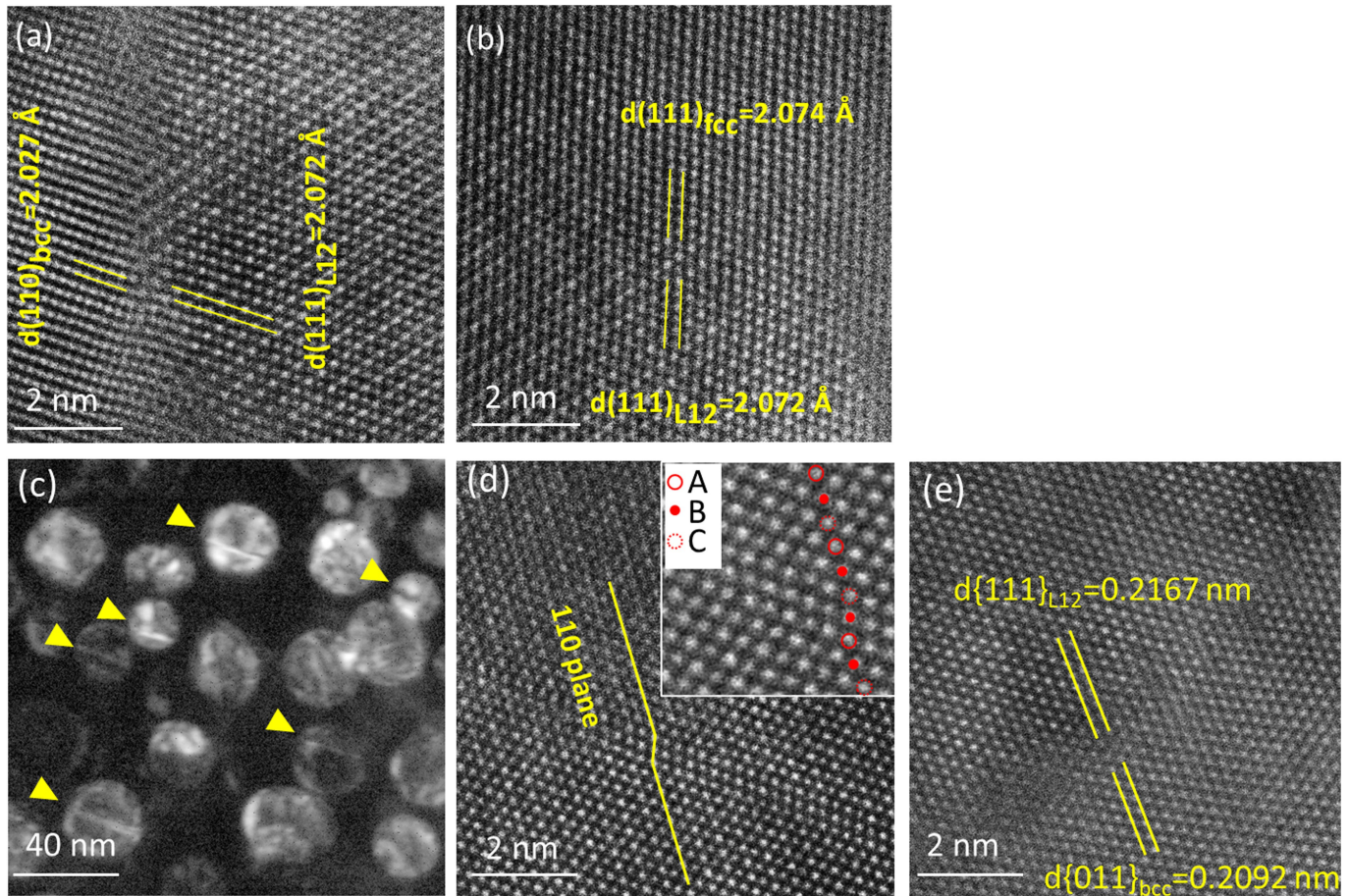
**Extended Data Fig. 1 | Temperature dependence of phase equilibria and composition calculated using the CALPHAD approach, and the free energy from first-principles calculations.** **a**, Mole fraction of equilibrium phases in

FNAT. **b**, Compositions of elements (at%) in the fcc phase. **c**, Free energy of fcc and bcc phases that have the same composition (Fe-23Ni-3.5Al-0.5Ti, at%) as the matrix of FNAT.



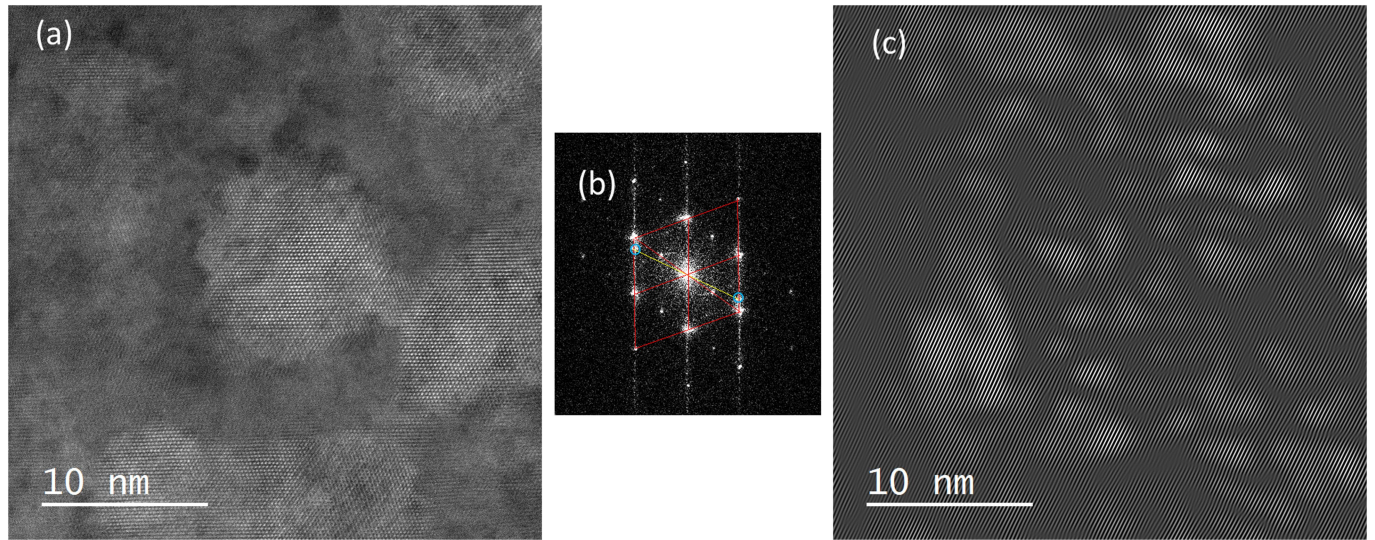
**Extended Data Fig. 2 | Information for estimating yield strength of FNAT-47h.** **a**, Room-temperature tensile stress–strain curve of FNAT after solutionizing at 1,100 °C and water quenching showing yield strength of

~325 MPa. **b**, STEM bright-field image showing dislocations cutting particles (yellow arrows) in the matrix of a plastically deformed FNAT sample. **c**, Corresponding HAADF image of **b**.



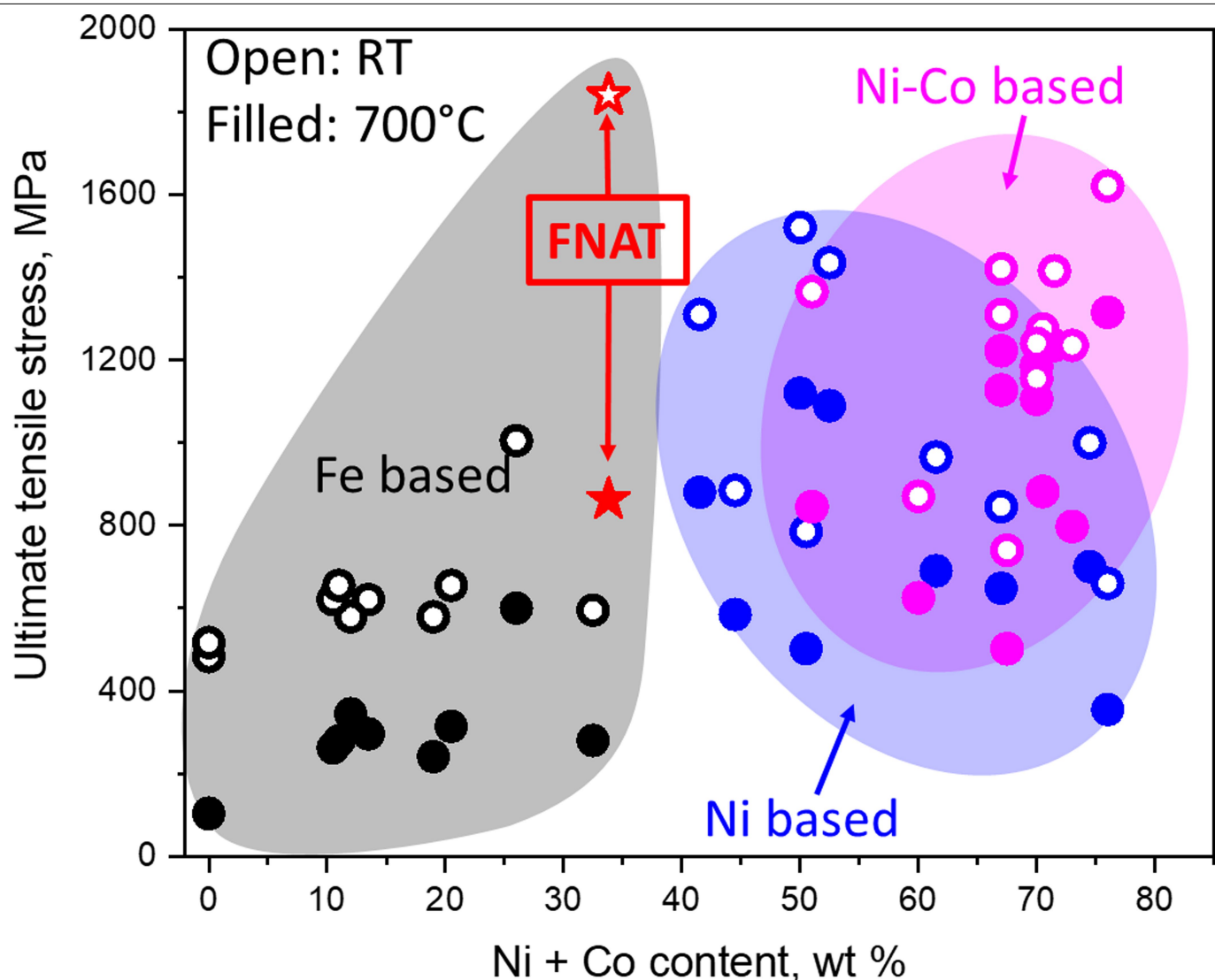
**Extended Data Fig. 3 | TEM/STEM analyses of interface between precipitate and matrix of the FNAT-47h alloy.** **a, b**, HAADF lattice images before deformation (from tab section of tensile specimen). **a**, A lattice image of L<sub>1</sub><sub>2</sub>/bcc interface displays the Nishiyama-Wasserman orientation ( $\bar{1}\bar{1}1$ )<sub>L<sub>1</sub><sub>2</sub></sub>||( $\bar{0}\bar{1}\bar{1}$ )<sub>bcc</sub> and [110]<sub>L<sub>1</sub><sub>2</sub></sub>||[100]<sub>bcc</sub>, where the interplanar spacings,  $d(\bar{1}\bar{1}1)_{L_1}=0.2072\text{ nm}$  and  $d(0\bar{1}\bar{1})_{bcc}=0.2027\text{ nm}$ , result in a mismatch of -2.2% and a semi-coherent interface. **b**, A lattice image of L<sub>1</sub><sub>2</sub>/fcc interface region exhibits full cube-on-cube lattice coherency with ( $\bar{1}\bar{1}1$ )<sub>L<sub>1</sub><sub>2</sub></sub>||( $\bar{1}\bar{1}1$ )<sub>fcc</sub> and [110]<sub>L<sub>1</sub><sub>2</sub></sub>||[110]<sub>fcc</sub>, where the interplanar spacings,  $d(\bar{1}\bar{1}1)_{L_1}=0.2072\text{ nm}$  and  $d(\bar{1}\bar{1}1)_{fcc}=0.2074\text{ nm}$ , result in a small mismatch of ~0.1%. **c–e**, TEM and HAADF lattice images after deformation (from gauge section of tensile specimen). **c**, Dark-field TEM image

showing L<sub>1</sub><sub>2</sub> precipitates, some containing streaks (marked by arrowheads), embedded in a deformation-induced bcc grain after deformation. **d**, HAADF lattice image showing a stacking fault with a Burgers vector of  $\frac{1}{6}<112>$  formed in one of the L<sub>1</sub><sub>2</sub> precipitates containing streaks. Labels A, B, C in the inset denote alternating {111} planes in the L<sub>1</sub><sub>2</sub> structure. **e**, HAADF lattice image showing semi-coherent L<sub>1</sub><sub>2</sub>/bcc interface with the Kurdjumov-Sachs orientation relationship<sup>64</sup>, namely, ( $\bar{1}\bar{1}1$ )<sub>L<sub>1</sub><sub>2</sub></sub>||( $\bar{1}\bar{1}0$ )<sub>bcc</sub> and [110]<sub>L<sub>1</sub><sub>2</sub></sub>||[111]<sub>bcc</sub> and a lattice mismatch of -2.2%. The slip-transfer mechanism in **c–e** is common when dislocations move from fcc matrix to L<sub>1</sub><sub>2</sub> precipitate, but is rarely seen when the matrix is bcc.



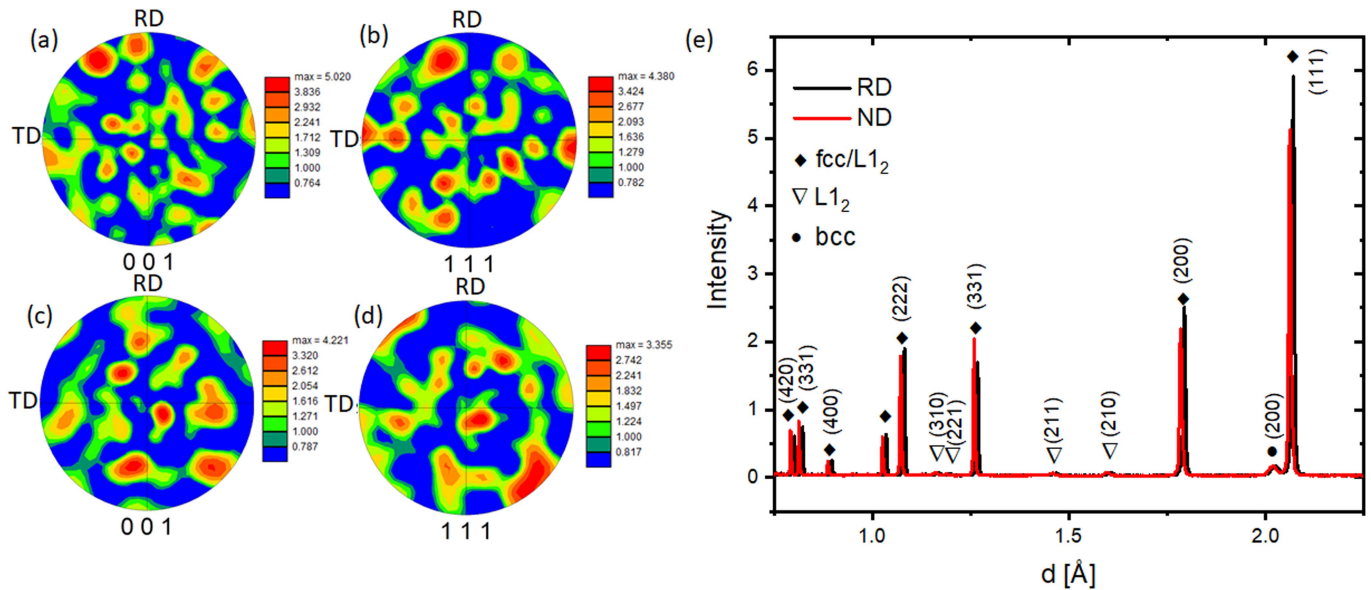
**Extended Data Fig. 4 | STEM HAADF image, corresponding FFT diffractogram and inverse FFT image of the as-quenched FNAT-4h alloy sample tilted to [110] zone axis condition. a, HRSEM image. b, FFT diffractogram. c, the inverse FFT generated using the blue-circled 'extra spots'**

in **b**. The diffuse spatial distribution of the bright features in **c** indicates that the extra spots in **b** are caused by small variable local misorientations due to local internal strains as opposed to any nano-domains of a different matrix phase.



**Extended Data Fig. 5 | Ultimate tensile strength versus Ni or (Ni + Co) content at room temperature and 700 °C.** Open symbols, room temperature (RT); filled symbols, 700 °C. The FNAT alloy is compared with different materials whose data sources are Fe-based heat-resistant alloys including 410, 430, 302, 309, 310, 316, 321, 347<sup>65</sup> A286 and Incoloy 800<sup>66</sup>; Ni-based super

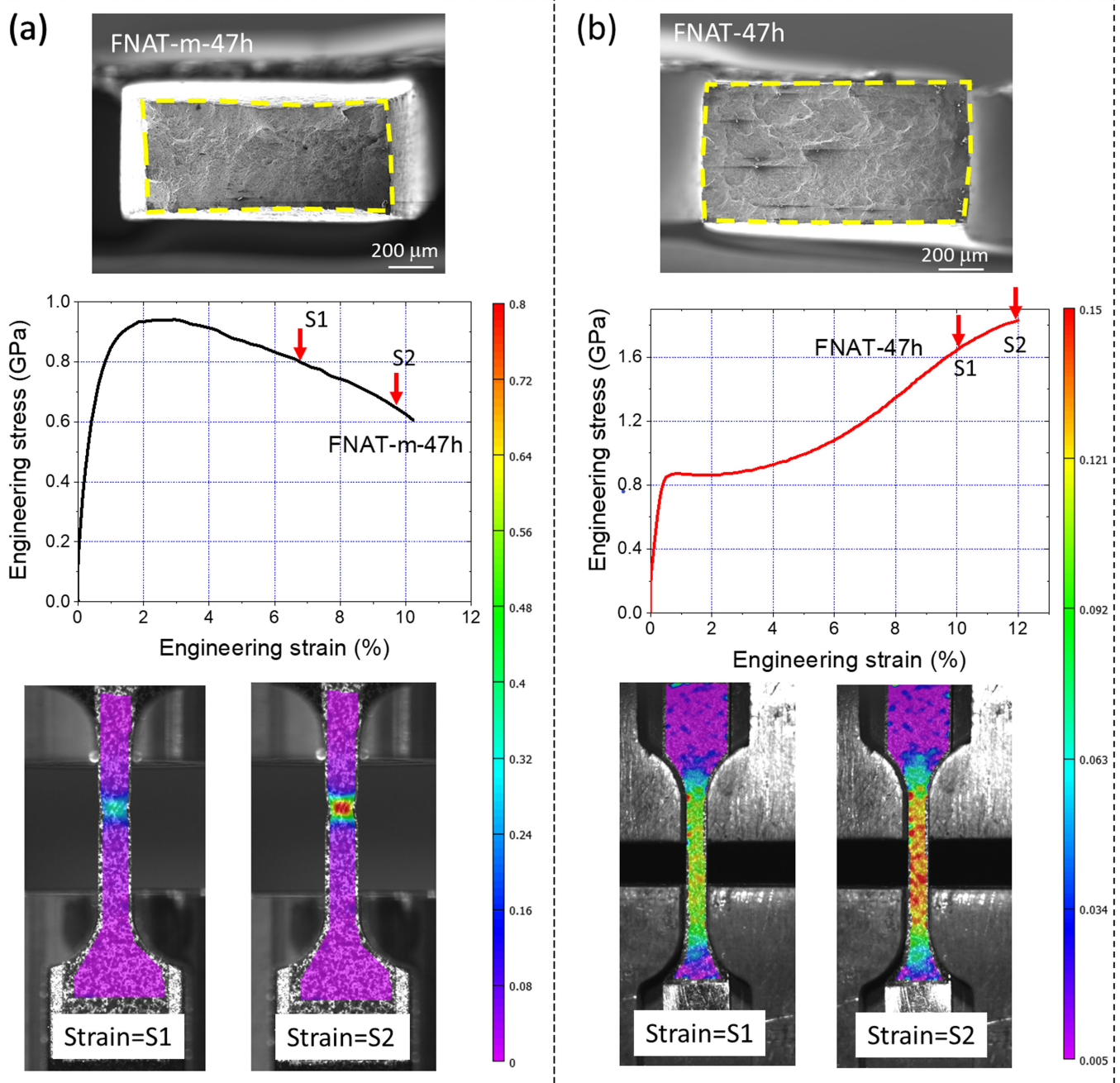
alloys<sup>66</sup> including Inconel 706, Inconel 718, Nimonic 80A, PE16, Inconel 625, Inconel 600, Hastelloy S, Hastelloy X, Udimet 630; and Ni–Co-based super alloys<sup>66</sup> including Incoloy 909, Nimonic 90, Nimonic 115, Waspaloy, Udiment 720, Udiment 500, Rene 41, Rene 95, Astroloy, Inconel 617 and Haynes 230.



**Extended Data Fig. 6 | Textures of FNAT-47h and FNAT-m-47h after hot-rolling and annealing.** **a, b,** EBSD pole figures for FNAT-47h, **c, d,** EBSD pole figures for FNAT-m-47h. The normal direction (ND) in each case is at the centre of the circle and is either 001 or 111 as marked. TD in **a–d** refers to the transverse direction. **e,** Neutron diffraction spectra of FNAT-47h along the

rolling direction (RD) and the normal direction (ND). Note that we have shifted the RD and ND spectra horizontally with respect to each other to facilitate comparison (otherwise the peaks would overlap). Both EBSD (**a, b**) and ND (**e**) results show that FNAT-47h has negligible texture.

# Article



**Extended Data Fig. 7 | Fracture analysis of tensile-tested FNAT-m-47h and FNAT-47h alloys.** **a**, FNAT-m-47h: fractograph and stress–strain curve showing considerable necking before fracture, and DIC strain maps showing strain localization in the region where fracture eventually occurs. **b**, FNAT-47h:

fractograph and stress–strain curve showing minimal necking before fracture, and DIC strain maps showing relatively diffuse strain distribution throughout the gauge section with no evidence of localization near the fracture plane.

**Extended Data Table 1 | Precipitate parameters calculated from different fits to APT data**

	Average radius (nm)	Root of mean square (nm)	Volume (nm <sup>3</sup> )	$I_0$ (cm <sup>-1</sup> )	$V_f$	Number density (#m <sup>-3</sup> )
Polydisperse sphere	10.4	2.5	$5.65 \times 10^3$	431	0.244	$4.31 \times 10^{22}$
Sphere	11.4	N/A	$6.11 \times 10^3$	255	0.21	$3.39 \times 10^{22}$
Ellipse	14.6, 9.92	N/A	$7.35 \times 10^3$	333	0.231	$3.14 \times 10^{22}$

$I_0$ , normalized scattering intensity when the scattering factor Q is zero;  $V_f$ , volume fraction; N/A, not applicable.

## Article

**Extended Data Table 2 | Parameters of precipitates in deformed and undeformed bcc and fcc grains**

Ni isosurface (%)	40	50	60
Average radius (nm)			
Deformed bcc	7.5	12.3	10.0
Deformed fcc	10.2	12.4	7.8
Undeformed bcc	12.7	12.2	11.5
Undeformed fcc	11.1	11.4	11.4
Volume fraction (%)			
Deformed bcc	36.7	31.5	26.6
Deformed fcc	36.7	31.4	26.5
Undeformed bcc	34.3	29.7	25.0
Undeformed fcc	34.4	30.3	25.6
Number density $\times 10^{22}$ (#/m <sup>3</sup> )			
Deformed bcc	2.12	2.71	3.09
Deformed fcc	1.83	1.40	3.41
Undeformed bcc	2.44	2.92	3.10
Undeformed fcc	1.84	2.46	3.02

Data derived from APT results using 40%, 50% and 60% Ni isosurfaces. The statistics suggest that the precipitate distribution is similar for all four cases listed in the first column for each specified isosurface. The larger the isosurface Ni concentration, the higher the number density and lower the volume fraction.